Comparison of Optimized Chargepads for Wireless EV Charging Application

Bandyopadhyay, Soumya; Dong, Jianning; Qin, Zian; Bauer, Pavol

DOI
10.23919/ICPE2019-ECCEAsia42246.2019.8796904

Publication date
2019

Document Version
Final published version

Published in
2019 10th International Conference on Power Electronics and ECCE Asia (ICPE 2019 - ECCE Asia)

Comparison of Optimized Chargepads for Wireless EV Charging Application

Soumya Bandyopadhyay*, Jianning Dong*, Zian Qin* and Pavol Bauer*
*Dept. Electrical Sustainable Energy, DCE&S group
TU Delft, Mekelweg 4, 2628 CD, Delft, the Netherlands
Email: s.bandyopadhyay-1@tudelft.nl, j.dong-4@tudelft.nl, z.qin-2@tudelft.nl, and p.bauer@tudelft.nl

***Abstract*—Inductive power transfer (IPT) is becoming increasingly popular in stationary electric vehicle charging systems. In this paper, the influence of the different IPT coupler geometries on the performance factors efficiency, power density, misalignment tolerance, and stray field is studied. Five different coupler topologies namely the circular, rectangular, double-D (DD-DD) and the double-D transmitter with double-D-Quadrature receiver (DD-DDQ) are considered in this study. The electromagnetic behavior of the couplers is modeled using three-dimensional finite element analysis. To ensure a fair quantitative comparison, a multi-objective optimization framework is developed to analyze the Pareto trade-offs between conflicting performance metrics like power densities, efficiencies, and misalignment tolerance for all the considered coupler topologies.**

I. Introduction

Inductive power transfer (IPT) is a popular solution for a wide range of battery charging applications, such as low power bio-medical implants, industrial automation, consumer electronics and electric vehicles (EVs) [1]. IPT technology for EV charging is more user-friendly and safe than conventional wired charging due to the absence of electrical or mechanical contacts. Additionally, it opens up the possibility of dynamically charging the EV battery while they are running [2], [3]. This solves two critical challenges associated with EVs: a) range anxiety which hinders proliferation of the EV market [4] and b) deep cycling of the battery which leads to its lifetime reduction [3]. Due to these advantages as mentioned above, IPT technology is a crucial enabling factor for a further increase in the popularity of EVs.

To match the plug-in charging efficiencies, IPT designs require highly efficient magnetic couplers. There is a large number of coupler topologies for IPT based EV charging reported in literature [5]–[8]. However, a proper classification structure to incorporate all possible topologies is still missing. Based on coil winding strategy, there can be two types of lumped IPT charge pads: a) Solenoid or double sided flux couplers [7], [9] and b) planar or single-sided flux couplers [5]. Planar couplers can be further classified into two families based on fundamental flux path: a) non-polarized couplers like circular and rectangular geometries [10]–[12] and b) multi-coil polarized couplers like double D (DD) [6], [13], double D-Quadrature (DDQ) [5], [14]. Comparisons between different concepts are found in several publications [16]–[19]. Several coil topologies are compared using numerical methods and statistical methods in [16], [17]. However, in that study different loss mechanisms in the charge pads are not considered. Also, the advantages of the various coil topologies about primary performance factors like power transfer efficiency, power densities, misalignment differences and stray field exposure are not clear.

This paper extends the above studies to include all major topologies and performance parameters. To compare the topologies, a 5 kW, 15 cm airgap IPT EV charging system is used as case study. The designs specifications include operation during extreme misalignment conditions. This provides the platform to compare the misalignment tolerance of the considered coupler topologies comprehensively. A four target multi-objective optimization is used to show the fundamental differences between the coupler topologies on different performance metrics. 3D finite element models are used to analyze the couplers, allowing all relevant electromagnetic losses to be considered. Experimental results are presented to validate the IPT coil models. Particle swarm algorithm (PSO) combined with Pareto dominance is used as the optimization algorithm [20]. Finally, the Pareto trade-offs are utilized to compare coupler topologies.

The paper is structured in five parts. Section II is about the classification of different coupler topologies based on their fundamental magnetic behavior. In the next section, the system modeling is discussed followed by another section on the multi-objective optimization (MOO) strategy. The optimization results are also discussed in detail. Finally, general conclusions are summarized based on the comparative analysis.

II. Classification of coil geometries

As previously highlighted, a significant number of IPT coil topologies are reported in the literature. Before the construction of a framework for comparative analysis, a classification strategy which includes most coil topologies is necessary to make the comparison insightful. Therefore, in this section, coupler topologies reported in the literature are presented in a classification structure based on winding strategy and flux path of the magnetic field.

A. Single-sided and double-sided couplers

IPT coils typically use ferrite bars to enhance coupling coefficient by shaping the magnetic field produced by the coils. The coil can be wound around the ferrite bars to channel the flux, resulting in a double-sided winding structure. The structure of double-sided winding resembles that of a flattened

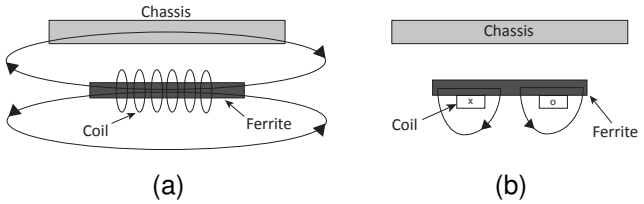

Figure 1. Classification of coupler topologies based on the strategy of coil winding: (a) double-sided winding, (b) single-sided winding.

solenoid (see Figure 1a). Alternatively, spiral planar coils can be placed on the ferrite material to produce magneto-motive force (MMF) only in one side, resulting in a single-sided winding or planar couplers (see Figure 1b). Comparative studies between solenoid couplers and planar couplers can be found in literature [5]. When a double-sided winding is used, the magnetic coupler can be made smaller than a transformer with a single-sided winding. However, double-sided winding transformers have a leakage flux at the back of the core, and consequently, they have low coupling factors. Therefore, this paper focuses on planar or single-sided flux couplers.

B. Single-sided coupler: Classification based on fundamental flux path

Single-sided couplers can be further classified into two types: polarized couplers and non-polarized couplers. Popular polarized and non-polarized couplers reported in the literature are namely the double-D (DD) and circular topologies [10] respectively. Other than circular topology, there also can be rectangular coils and square coil topologies (can be considered as a particular case of rectangular coils). The fundamental difference between polarized and non-polarized couplers is the nature of the magnetic flux path. To illustrate the difference between the couplers, the fundamental flux paths of both coupler types are shown and explained in Figure 2.

C. DD polarized couplers: Classification based on receiver types

Polarized couplers can be further classified into three types depending on the receiver coil topology: (a) double-D planar (DD) receiver, (b) double-D-quadrature planar (DDQ) receiver, and (c) bi-polar pad (BPP) receiver. DD receiver has same structure as the DD primary (see Figure 2). Both DDQ and BPP coil topologies improve misalignment performance of a DD receiver. DDQ receiver has a Q coil symmetrically placed on the DD structure. The Q coil is magnetically decoupled from the DD structure due to its inherent spatial positioning. This enables individual tuning and control of the DD coils and the Q coil depending on alignment conditions. A similar decoupling strategy is exploited in BPP receivers. The overlap between the two coils is designed to ensure zero (as close to zero as practically possible) mutual coupling between them. The extent of overlap needed between the coils to ensure decoupling depends on the overall charge pad structure [14]. However, determining the overlapping extent needs an experimental

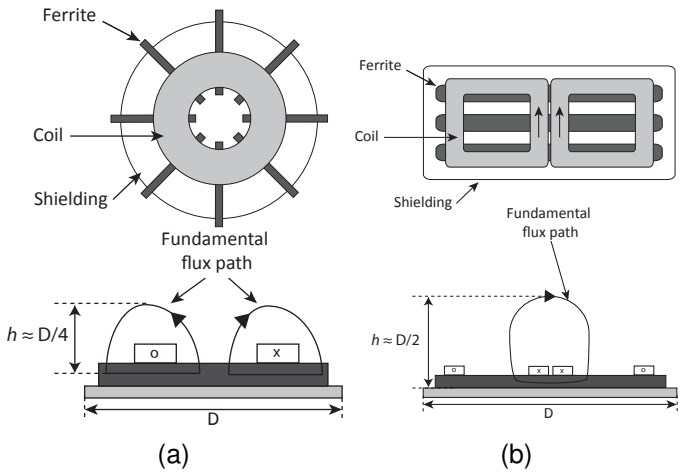

Figure 2. Classification of coupler topologies based on fundamental flux path:(a) Non-polarized coupler has a symmetric magnetic field around its center point, the fundamental flux height (h) is roughly proportional to a quarter of pad diameter ($h \approx \frac{D}{4}$), and (b) Polarized coupler has magnetic flux travelling along the length of the pad, the the fundamental flux height (h) is roughly proportional to half of the pad length ($h \approx \frac{D}{2}$).

approach or an iterative approach [6]. The overall IPT coil topology classification is presented based on the strategy discussed in this section. Based on the presented qualitative arguments, the following promising coil topologies are selected for detailed comparative analysis:

1) Circular (Transmitter + Receiver)
2) Rectangular (Transmitter + Receiver)
3) DD (Transmitter + Receiver)
4) DD (Transmitter) - DDQ (Receiver)
5) DD (Transmitter) - BPP (Receiver)

III. System Overview and Analysis

The overall IPT system for EV charging is briefly presented in this section followed by the modelling strategy. Figure 3 shows the overall IPT system which consists of mainly five power conversion stages from the power source to the load or battery. In this paper, we will focus on the middle three conversion stages: (a) dc-ac converter, (b) the magnetic link, and (c) ac-dc converter.

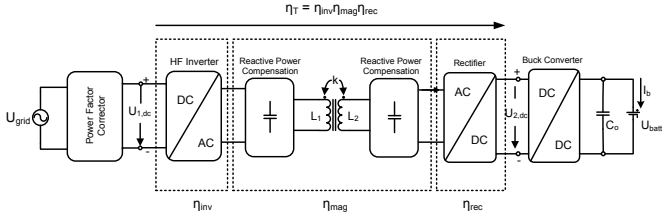

Figure 3. The overall IPT system for EV charging from the grid to the battery is presented. In this paper, the efficiency of power transfer from the transmission side dc link ($U_{1,\mathrm{dc}}$) to the receiver side dc link ($U_{2,\mathrm{dc}}$).

A. 3D Axi-symmetric FE Modelling

The couplers selected for comparative analysis in the previous section will be modeled and analyzed in this section. Finite element (FE) analysis is used to model the coupler electromagnetics. The resulting data is post-processed to extract the losses in the coupler along with other performance metrics. Finally, the control strategy for the IPT system during aligned and misaligned conditions is discussed. COMSOL, a commercially available FE software is used to model the couplers. The considered couplers consist of distributed ferrite strips. Hence, 3D finite element (FE) models are necessary to compute their electromagnetic behavior. However, this leads to the longer computation time for individual models. To make the 3D models suitable for optimization purposes, geometrical symmetries of the couplers are exploited to reduce the computation time. A combination of symmetry boundary conditions like the parallel flux, normal flux, and periodic boundary conditions [22] are used to reduce the computational loads of the 3D models by several orders. Figure 4 presents the model computational load reduction technique for polarized-DD and circular coils.

B. Compensation and Control strategy

Series-series compensation is chosen due to its theoretically low sensitivity to coil misalignment [21]. However, in practice, the resonant frequency of the IPT system changes during misalignment due to the change in the primary inductance [23].

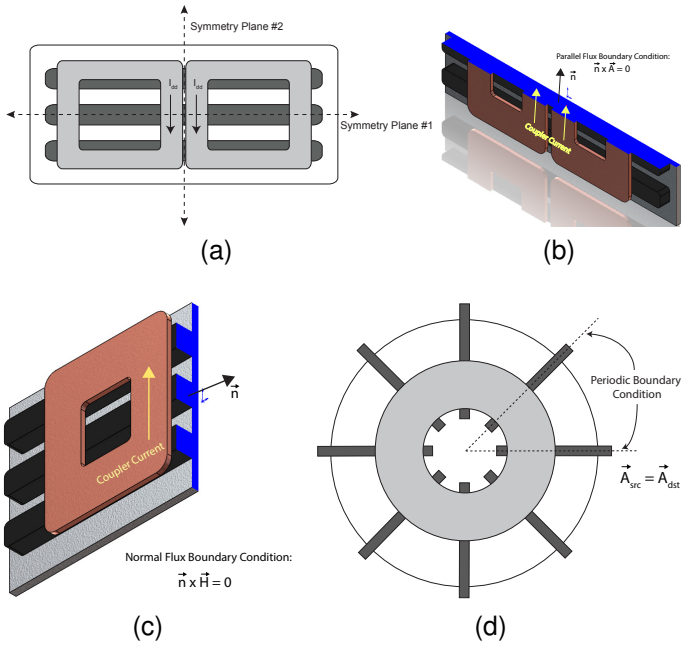

Figure 4. (a) Axes of symmetries in a polarized DD coupler, (b) Symmetry Plane 1: Parallel flux boundary condition is applied along the axis of the central core strip, (c) Symmetry Plane 2: Normal flux boundary condition is applied along the axial plane between the two D coils, (d) A periodic boundary condition is applied along the axis of two ferrite strips in case of a circular coupler. The model reduction order is the number of ferrite strips in the coupler.

Series-series compensation strategy for multi-coil coupler families like DD-DDQ and DD-BPP is shown in Figure 5.

A dual sided control strategy is considered in this paper. The transmitter coils are excited by a high-frequency square-wave inverter. The power is controlled by varying the transmitter side dc voltage $U_{1,dc}$ (Figure 3). The dc link voltage ($U_{2,dc}$) in the pickup circuit is controlled by a dc-dc converter before the battery. A detailed analysis of this control strategy is already presented in [24] for further reference. Based on that, the power transfer to the pick-up circuitry can be written as:

$$P_{\text{out}} = \frac{8}{\pi^2} \frac{U_{1,\text{dc}} U_{2,\text{dc}}}{\omega M} \tag{1}$$

where P_{out} is the reference power requested by the battery, ω is the angular frequency of the system, M is the mutual inductance between the couplers. To improve efficiency performance during both aligned and mis-aligned conditions, the optimal load impedance matching algorithm [21] is used which results in maximum power transfer efficiency for a particular coupling k. Accordingly, the reference value of the receiver dc link voltage $U^*_{2,\text{dc}}$ (see Figure 3) during load impedance matching is determined using the following equation:

$$U^{*2}_{2,\text{dc}} \approx \frac{\pi^2}{8} \eta_{\text{rec}} \omega M P_{\text{out}} \sqrt{\frac{r_{\text{acR}}}{r_{\text{acT}}}} \tag{2}$$

where r_{acT} and r_{acR} are the ac resistances of the transmitter and receiver couplers. Therefore, $U^*_{2,\text{dc}}$ is used as a set point to ensure maximum power transfer efficiency. To ensure power regulation, the set point value of the transmitter side dc link voltage $U^*_{1,\text{dc}}$ is calculated based on the set point $U^*_{2,\text{dc}}$. The derivation of (2) is shown in the appendix.

During misalignment the value of M changes which will lead to the change of set point value of $U^*_{2,\text{dc}}$. Active impedance matching can still be executed on real time with a new estimate of mutual inductance (M′) and the new set point for the secondary dc link voltage will then be:

$$U^{'*}_{2,\text{dc}} = U^*_{2,\text{dc}} \sqrt{\frac{M'}{M}} \tag{3}$$

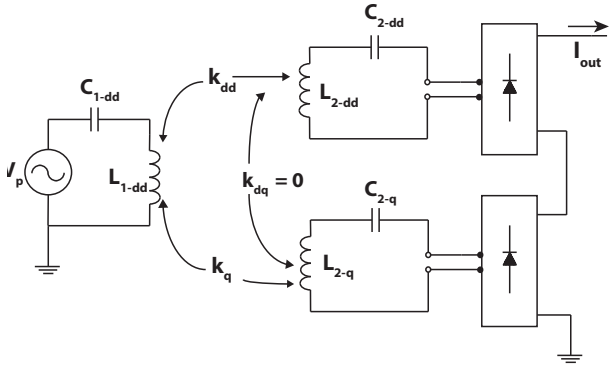

Figure 5. Series-series compensation strategy for multi-coil topologies like DD-DDQ coil based IPT system. Similar compensation strategy is used for DD-BPP IPT system.

During operation, the coupling co-efficient (k) or the mutual inductance can be estimated online by measuring the voltages and currents of the transmitter and receiver pads:

$$k = \frac{V_{\mathrm{p}} + \sqrt{V_{\mathrm{p}}^2 - 4r_{\mathrm{acT}} I_{\mathrm{s}}(V_2 + I_{\mathrm{s}} r_{\mathrm{acR}})}}{2I_{\mathrm{s}}\omega_{\mathrm{o}}\sqrt{L_{\mathrm{p}} L_{\mathrm{s}}}} \tag{4}$$

where V_{p}, V_{s} are the transmitter and receiver side ac rms voltages.

C. System Losses

System losses in a wireless IPT system is mainly comprised of electro-magnetic losses incurred in the couplers and the losses in the power electronic converters like the high-frequency inverter and the power rectifier. The aforementioned losses are discussed briefly in the following.

1) Chargepad and compensation Losses: The main source of losses in the couplers are due to (a) dc+ac copper losses, (b) ferrite losses, (c) shielding losses, and (d) dielectric losses. These loss mechanisms in magnetic chargepads have been investigated thoroughly in existing literature [12], [21], [24], [25].

2) Power Electronic Losses: The power electronic losses include the losses in the inverter and the rectifier ($P_{\mathrm{inv}}, P_{\mathrm{rec}}$). SiC Schottky diodes (C4D40120D) and MOSFET (C2M0025120D) by Cree are considered for the device loss models. The switching and conduction losses are computed using the data provided in the manufacturer's datasheet and equations presented in [26]. The total system transmission efficiency η_{T} is then determined by the following equation:

$$\eta_T = \eta_{\mathrm{inv}}\eta_{\mathrm{mag}}\eta_{\mathrm{rec}} = \frac{P_{\mathrm{out}}}{P_{\mathrm{out}} + P_{\mathrm{tot}} + P_{\mathrm{inv}} + P_{\mathrm{rec}}} \tag{5}$$

where P_{out} is the power ouput computed at the terminals of the rectifier, η_{inv} , η_{rec}, η_{mag} are the efficiencies of the inverter, rectifier, and couplers respectively.

IV. Optimization Framework

A multi-objective optimization framework is developed in this section to compare the chosen coupler concepts. It utilizes the numerical modeling strategy developed in Section III-A to evaluate the performance of the couplers.

A. Optimization targets, and system specifications

The coupler concepts are compared on the primary performance factors like efficiency, power densities, and misalignment performance. Based on that, the targets of the optimization are:

1) Maximize power transmission efficiency (η_{T})
2) Maximize gravimetric power density (γ)
3) Maximize receiver pad area power density (α)
4) Maximize efficiency during misalignment (η_{mis})

The objectives mentioned above are selected strategically to ensure that the optimization progresses towards designs with acceptable power densities and efficiency performance during both aligned and misaligned conditions. Table I shows the IPT system specifications. The optimization algorithm used for this problem is particle swarm optimization (PSO). PSO is an evolutionary gradient free algorithm inspired by the movement of birds or insects in swarm which is gradient free and potentially requires fewer function calls [27]. In this paper, an approach based on placing particles on the border of the search space using a combination of variable clipping and reflecting [27].

Table I
IPT SYSTEM SPECFICATIONS

Symbol	Description	Value
δ	Operational air-gap	15 cm
$\mathrm{P_{out}}$	Battery power requirement	5 kW
f	Operational frequency	85 kHz
$\mathrm{U_{batt}}$	Nominal battery voltage	400 V
$\mathrm{U_{1,dc}}$	Input dc link voltage	850 V
$\mathrm{U_{2,dc}}$	Pick up dc link voltage	400-850 V
Δx	Lateral misalignment	$\pm$ 15 cm
Δy	Longitudinal misalignment	$\pm$ 15 cm

B. Optimization variables, and constraints

The design variables of the optimization problem are all geometrical parameters of different coupler structures as shown in Figure 6. Ten geometrical parameters per coupler pad (transmitter and receiver) are optimized to ensure high design flexibility and exhaustive design space exploitation. The optimization variables and their range are presented in Table II.

To ensure feasible designs, specific constraints are put on the optimization solution space. A hard limit of 5A/mm^2 is placed on the litz wire current density to ensure thermal stability. The maximum flux density and the average flux density in the ferrite cores during misalignment operation is set to be 0.35 T and 0.2 T respectively (saturation flux density for 3C-90 core material is 0.45 T).

This concludes the development of the MOO framework consisting of 20 design variables, 4 performance targets, and 6 constraints. The overall optimization is computationally expensive and requires solving 3000-4000 designs to arrive at stable Pareto fronts. The optimization results are discussed in the next section.

V. Results of Optimization

The multi-objective optimization framework results in a 4D Pareto optimal front which is challenging to present. To aid visualization and insight into the results, a detailed analysis is conducted in three steps. First, Pareto front analysis of performance targets during perfect alignment are shown. Second, similar analysis is performed on performance targets during misalignment. Finally, optimized designs from different coupler families are chosen with similar power densities and their overall performance is analyzed in detail.

Figure 7 and Figure 8 show the side views of the 4D Pareto optimal front which highlight the trade-offs between efficiency at alignment, efficiency at misalignment, and power

[1] 100% means the outermost ferrite strips are at the edge of the coupler and 0% represents that all the ferrites are together forming a block in the center.
[2] Represented as a percentage of the total coil length.

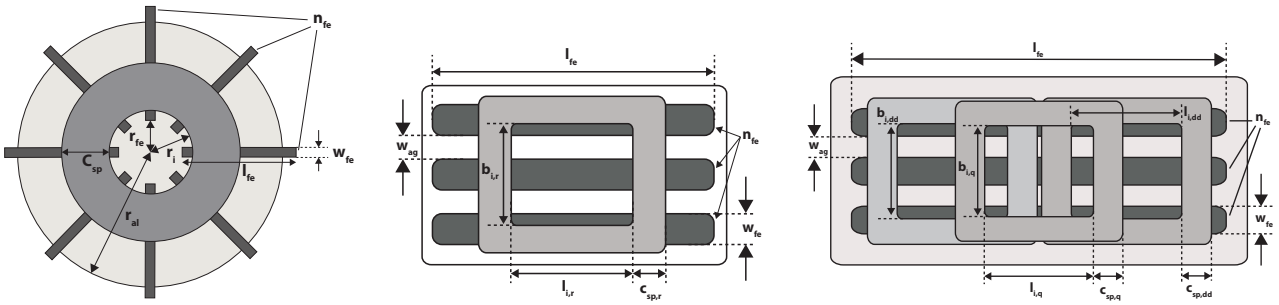

Figure 6. Design variables for (a) Circular coupler, (b) rectangular coupler and (c) DDQ receiver pad topology. In the figures, the ferrite thickness (h_{fe}) is a variable which is not shown. The optimization variables of DD-DD and DD-BPP are similar to that of DDQ with the exception of the extra variables due to the Q coil. The coil spread parameter (C_{sp}) is defined as: $C_{\text{sp}} = N \times d$, where N is the number of turns and d is the external diameter of the litz wire which depends on the number of strands (n_{str}).

Table II
OPTIMIZATION VARIABLES AND THEIR RANGE

Variable	Symbol	Unit	Range				
			DD-DD	DD-BPP	DD-DDQ	Rect	Circ
Number of turns	N_{T}, N_{R}	-	15-60	15-60	15-60	20-65	20-65
Number of turns in Q coil	N_{Q}	-	-	-	15-60	-	-
Diameter of litz wire	d_{litz}	mm	2.4 - 4.8	2.4 - 4.8	2.4 - 4.8	2.4 - 4.8	2.4 - 4.8
Inner length	l_{i} , r_{i}	mm	10-35	10-35	10-35	10-75	10-75
Inner width	w_{i}	mm	10-35	10-35	10-35	10-75	-
Ferrite thickness	h_{fe}	mm	5-35	5-35	5-35	5-35	5-35
Ferrite width	w_{fe}	mm	15-45	15-45	15-45	15-45	15-45
Gap between ferrites[1]	w_{ag}	%	20-100	20-100	20-100	20-100	-
Length of ferrite [2]	l_{fe}	%	50-120	50-120	50-120	50-120	50-120
Number of ferrites	n_{fe}	-	1-7	1-7	1-7	1-7	2-12

densities. To distinguish between the coupler shapes, only the sub-fronts are shown. These plots show the maximum achievable performance in one parameter only, disregarding the performance on other parameters. It means that the designs located on, e.g., the $\eta - \gamma$ sub-front do not necessarily lie on the $\eta_{\text{mis}} - \alpha$. However, this representation can reveal strong or weak coils based on the goals, as well as provide insight into the limits of the performance goals individually.

A. Pareto Front analysis of designs during alignment

Figure 7a show the Pareto fronts of efficiency during perfect alignment versus gravimetric power density of the couplers. The circular coupler is the best performer in this particular metric closely followed by DD-DD couplers. Rectangular couplers perform comparatively poorly compared to different coils in the η - γ front, due to the mismatch between the linear alignment of the ferrite strips and the fundamental flux pattern associated with a unipolar rectangular coil. However, DD-BPP and DD-DDQ couplers perform the poorest among the selected coupler topologies with BPP slightly being better than DDQ. The polarized DD-DD couplers perform better than their rectangular counterpart in the $\eta - \gamma$ Pareto front since their fundamental flux pattern match with the linear arrangement of the ferrite strips in the polarized couplers. The dominance of circular couplers and the relative poor performance of DD-BPP and DD-DDQ in this performance metric can be explained by the amount of ferrite material used in the couplers. Circular couplers utilizes more ferrite material for the same gravimetric power density compared to other coils which lead to comparatively lower average flux density (B_{avg}) in the ferrite strips, thus leading to lower ferrite core losses.

Figure 7b shows the Pareto fronts of efficiency versus receiver area power density. The non-polarized couplers perform much better than the polarized family in this performance metric. Higher coupling coefficients associated with non-polarized couplers for the same receiver pad area compared to their polarized counterpart (see Figure 7c) results in lower driving currents for the same power transfer thus leading to lower losses. It is evident from Figure 7c, that circular and rectangular couplers show higher attainable coupling k during aligned conditions for the same area power density (α) than bi-polar couplers like DD-DD and DD-DDQ which is in accordance with the results reported in [12], [16], [17]. Within the non-polarized family, circular couplers perform better than the rectangular couplers due to slightly lower copper losses.

B. Pareto Front analysis of designs during mis-alignment

Figure 8a shows the η_{mis}-γ front for all the coupler geometries. DD-BPP couplers is the best performer by a significant margin in this metric compared to all the selected coil topologies. Circular coils come second in this metric followed by DD-DD in the third, DD-DDQ in fourth and rectangular couplers at the last. Rectangular couplers perform poorly in this metric similar to their performance in the $\eta_{\text{T}} - \gamma$

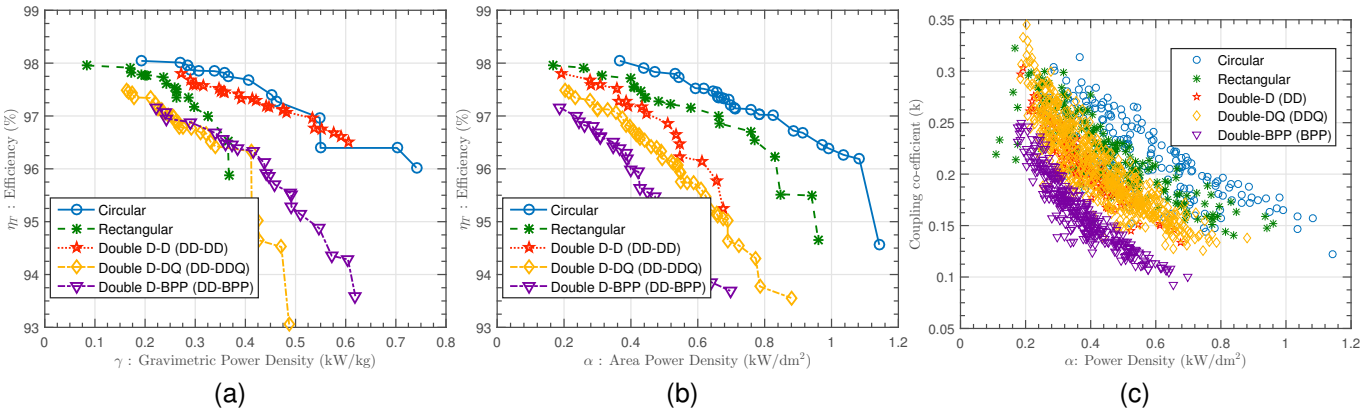

Figure 7. Results of multi-objective optimization during perfect alignment operating conditions: (a) $\eta_T - \gamma$: pareto fronts of trade off between efficiency and gravimetric power density, (b) $\eta_T - \alpha$: pareto fronts of trade off between efficiency and receiver area power density, (c) coupling coefficient of pareto designs vs receiver area power density.

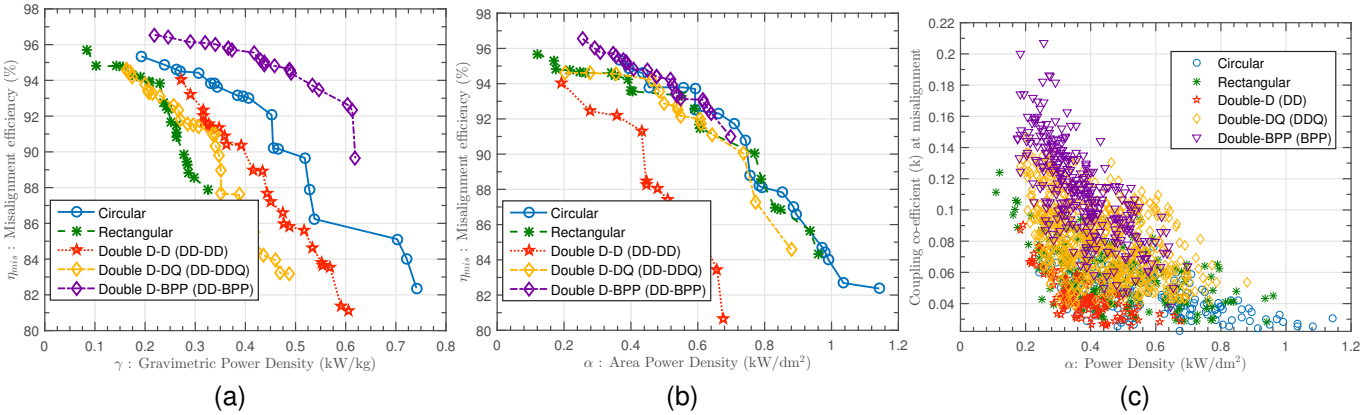

Figure 8. Results of multi-objective optimization during misaligned operating conditions: (a) $\eta_{\text{mis}} - \gamma$: pareto fronts of trade off between misaligned efficiency and gravimetric power density, (b) $\eta_{\text{mis}} - \alpha$: pareto fronts of trade off between misaligned efficiency and receiver area power density, (c) coupling coefficient of pareto designs vs receiver area power density during misaligned conditions.

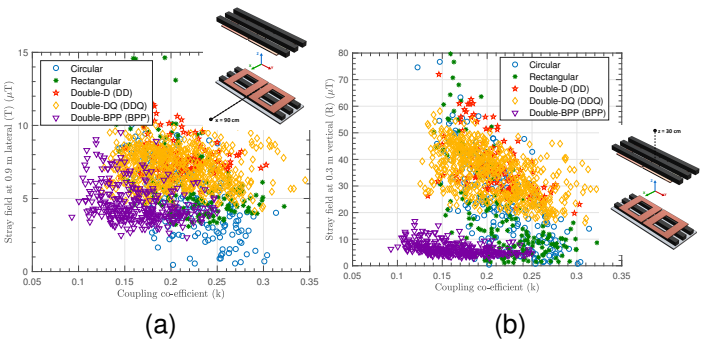

Figure 9. Stray field behavior of different coil concepts during perfectly aligned operation with coupling coefficient: (a) Stray field computed at 0.9 m lateral (x-direction) from the transmitter coil center, and (b) Stray field computed at 0.3 m vertical (z-direction) from the receiver coil center. The aluminum shielding on the receiver pad is not shown but considered.

sub-front. Figure 8b presents the $\eta_{\text{mis}} - \alpha$ front of the different coupler geometries. Similar to the $\eta_{\text{mis}} - \gamma$ front, the DD-BPP coupler family performs the best among the selected topologies. However, all the other couplers except the DD-DD family performs equally well. The dominance of DD-BPP coupler in all Pareto fronts regarding mis-alignment performance can be explained by the complementary flux capturing of the BPP coils which leads to high coupling coefficients even during msialignment (Figure 8c).

C. *Leakage fluxes*

The stray magnetic field generated by IPT couplers should comply with the guidelines set by ICNIRP [29]. Researchers have chosen different spatial points for spot leakage field measurements [12], [30]. In this paper, two points are taken for spot flux density computation: (a) 30 cm from the receiver coil center in the vertical direction (z) and, (b) 90 cm from the transmitter coil center on the lateral direction (y). The stray flux densities of the Pareto designs for the different coils with coupling coefficient are shown in Figure 9. In the lateral direction of the transmitter, DD-BPP and circular coils perform the best while DD-DD and DD-DDQ lag behind. In the vertical

direction, DD-BPP is again the best performer followed by the non-polarized couplers like circular and rectangular.

D. Comparison of selected designs

In this section, detailed analysis on selected designs will be conducted to gain deeper insights into the performance trends discussed in the previous results. Since the couplers are optimized with different conflicting objectives, it is difficult to select a single optimized design from each coupler family. To ensure a fair comparison, optimized couplers of similar power densities are selected and compared in detail. Figure 10 shows the selected particles in the 2D power denisty plot of all the Pareto dominant designs.

Table III shows in-depth results of the selected optimized designs of different coupler concepts. All the selected coupler designs have a receiver power density of 0.5 kW/dm^2 and system gravimetric power density of 0.3 kW/kg. The circular design performs the best in terms of both efficiency during alignment and efficiency during misalignment. In addition to that, the circular coupler design uses minimum copper material whereas DD-DDQ and rectangular design uses the highest amount of copper.

The variation of coupling coefficient of the selected coupler designs due to misalignment in longitudinal and lateral direction are shown in Figure 11. In case of lateral misalignment in the x-direction, rectangular couplers show better tolerance than circular and other polarized couplers. The polarized couplers perform much better in longitudinal misalignment with DD-DDQ showing the most resilience followed by DD-BPP.

VI. Conclusion

This paper presents a holistic comparison of four coupler concepts: circular, rectangular, DD-DD, DD-DDQ, and DD-BPP. 3D FE modelling is used to model the electromagnetic behavior of the couplers. To ensure a fair comparison, a multi-objective optimization approach is used to optimize different couplers types with different performance objectives like efficiency, misalignment tolerance, stray fields, and power densities.

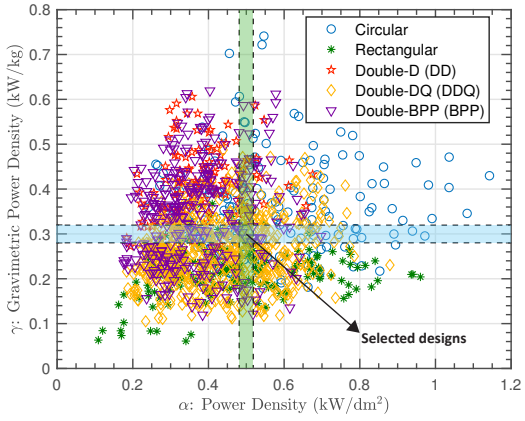

Figure 10. Selected non-dominated designs of all the coupler families based on gravimetric and area power density.

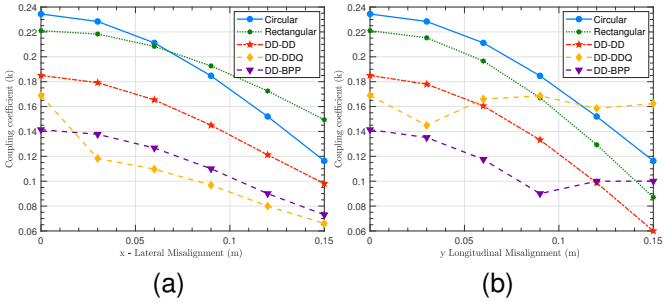

Figure 11. Variation of coupling coefficient during: (a) misalignment in the lateral direction, (b) misalignment in the longitudinal direction

During aligned operating conditions, circular coupler performs the best with highest efficiencies and low copper usage compared to the other couplers. Additionally, the circular couplers have the lowest leakage fields in the lateral direction. However, during misaligned conditions, the complementary nature of the pick up coils of DD-BPP leads to the best performance in terms of efficiency for the same gravimetric power density. Additionally, DD-BPP has the lowest leakage fields in the vertical direction among all the couplers. In conclusion, it is recommended to use circular couplers if the operating requirements of couplers doesn't include misalignment. However, if operating conditions require good performance during misalignment conditions, DD-BPP is the recommended coupler choice.

References

[1] D. Patil, M. K. McDonough, J. M. Miller, B. Fahimi, and P. T. Balsara, "Wireless power transfer for vehicular applications: Overview and challenges," *IEEE Transactions on Transportation Electrification*, vol. 4, no. 1, pp. 3–37, 2018.

[2] G. A. Covic and J. T. Boys, "Modern trends in inductive power transfer for transportation applications," *IEEE Journal of Emerging and Selected topics in power electronics*, vol. 1, no. 1, pp. 28–41, 2013.

[3] S. Jeong, Y. J. Jang, and D. Kum, "Economic analysis of the dynamic charging electric vehicle," *IEEE Transactions on Power Electronics*, vol. 30, no. 11, pp. 6368–6377, 2015.

[4] S. Chopra and P. Bauer, "Driving range extension of ev with on-road contactless power transfera case study," *IEEE transactions on industrial electronics*, vol. 60, no. 1, pp. 329–338, 2013.

[5] M. Budhia, J. T. Boys, G. A. Covic, and C.-Y. Huang, "Development of a single-sided flux magnetic coupler for electric vehicle ipt charging systems," *IEEE Transactions on Industrial Electronics*, vol. 60, no. 1, pp. 318–328, 2013.

[6] G. A. Covic, M. L. Kissin, D. Kacprzak, N. Clausen, and H. Hao, "A bipolar primary pad topology for ev stationary charging and highway power by inductive coupling," in *Energy Conversion Congress and Exposition (ECCE)*, pp. 1832–1838, IEEE, 2011.

[7] S. Raabe, G. Elliott, G. Covic, and J. Boys, "A quadrature pickup for inductive power transfer systems," in *Industrial Electronics and Applications,ICIEA*, pp. 68–73, IEEE, 2007.

[8] S. Y. Jeong, S. Y. Choi, M. Sonapreetha, and C. T. Rim, "Dq-quadrature power supply coil sets with large tolerances for wireless stationary ev chargers," in *Emerging Technologies: Wireless Power (WoW), IEEE PELS*, pp. 1–6, IEEE, 2015.

[9] Y. Nagatsuka, N. Ehara, Y. Kaneko, S. Abe, and T. Yasuda, "Compact contactless power transfer system for electric vehicles," in *Power Electronics Conference (IPEC)*, pp. 807–813, IEEE, 2010.

[10] M. Budhia, G. A. Covic, and J. T. Boys, "Design and optimization of circular magnetic structures for lumped inductive power transfer systems," *IEEE Transactions on Power Electronics*, vol. 26, no. 11, pp. 3096–3108, 2011.

Table III
COMPARISON OF OPTIMIZED COUPLERS

Performance Group	Performance Metrics	Symbol	Unit	Circular	Rectangular	DD-DD	DD-DDQ	DD-BPP
Coupler Sizing	Receiver area power density	α	kW/dm^2	0.5	0.48	0.5	0.5	0.5
	Gravimetric power density	γ	kW/kg	0.28	0.3	0.322	0.29	0.29
	Copper weight	W_{cu}	kg	1.7	4.3	2.4	4.8	2.2
	Ferrite weight	W_{fe}	kg	13.3	7.8	10.6	9.7	12
	Receiver weight	W_{rec}	kg	9	5.8	2.7	5	6.1
	Transmitter weight	W_{tr}	kg	8.8	11	13	12	11.3
Performance during alignment	Magnetic link Efficiency	η_{T}	%	98.6	97.7	98	97.8	97
	Coupling co-efficient	k	-	0.23	0.22	0.18	0.17	0.15
	Ferrite average flux density	B_{avg}	mT	75	120	90	80	120
	Ferrite loss	P_{fe}	W	7	46	17	22	31
	Copper loss	P_{cu}	W	13	19	26	26	43
	Capacitor loss	W_{cap}	W	46	46	57	64	74
	Shielding loss	W_{al}	W	5	4	4	5	3
	Stray Vertical	B_{vert}	μT	16	17	57	43	13
	Stray Lateral	B_{lat}	μT	4	6	9	9	7
Performance during misalignment	Magnetic link Efficiency	η_{mis}	%	93.4	90.7	89.9	93.1	91.1
	Coupling co-efficient	k_{mis}	-	0.05	0.06	0.04	0.08	0.05

[11] G. Buja, M. Bertoluzzo, and K. N. Mude, "Design and experimentation of wpt charger for electric city car," *IEEE Transactions on Industrial Electronics*, vol. 62, no. 12, pp. 7436–7447, 2015.

[12] R. Bosshard and J. W. Kolar, "Multi-objective optimization of 50 kw/85 khz ipt system for public transport," *IEEE Journal of Emerging and Selected Topics in Power Electronics*, vol. 4, no. 4, pp. 1370–1382, 2016.

[13] G. R. Nagendra, G. A. Covic, and J. T. Boys, "Determining the physical size of inductive couplers for ipt ev systems," *IEEE Journal of Emerging and Selected Topics in Power Electronics*, vol. 2, no. 3, pp. 571–583, 2014.

[14] A. Zaheer, D. Kacprzak, and G. A. Covic, "A bipolar receiver pad in a lumped ipt system for electric vehicle charging applications," in *Energy Conversion Congress and Exposition (ECCE)*, pp. 283–290, IEEE, 2012.

[15] S. Bandyopadhyay, V. Prasanth, L. R. Elizondo, and P. Bauer, "Design considerations for a misalignment tolerant wireless inductive power system for electric vehicle (ev) charging," in *Energy Conversion Congress and Exposition (ECCE)*, pp. 1–10, IEEE, 2017.

[16] K. Knaisch and P. Gratzfeld, "Comparison of magnetic couplers for inductive electric vehicle charging using accurate numerical simulation and statistical methods," in *Electric Drives Production Conference (EDPC)*, pp. 1–10, IEEE, 2015.

[17] K. Knaisch, M. Springmann, and P. Gratzfeld, "Comparison of coil topologies for inductive power transfer under the influence of ferrite and aluminum," in *Ecological Vehicles and Renewable Energies (EVER)*, pp. 1–9, IEEE, 2016.

[18] V. Prasanth, S. Bandyopadhyay, P. Bauer, and J. A. Ferreira, "Analysis and comparison of multi-coil inductive power transfer systems," in *Power Electronics and Motion Control Conference (PEMC)*, pp. 993–999, IEEE, 2016.

[19] R. Bosshard, U. Iruretagoyena, and J. W. Kolar, "Comprehensive evaluation of rectangular and double-d coil geometry for 50 kw/85 khz ipt system," *IEEE Journal of Emerging and Selected Topics in Power Electronics*, vol. 4, no. 4, pp. 1406–1415, 2016.

[20] C. A. C. Coello, G. T. Pulido, and M. S. Lechuga, "Handling multiple objectives with particle swarm optimization," *IEEE Transactions on evolutionary computation*, vol. 8, no. 3, pp. 256–279, 2004.

[21] R. Bosshard, J. W. Kolar, J. Mühlethaler, I. Stevanović, B. Wunsch, and F. Canales, "Modeling and pareto optimization of inductive power transfer coils for electric vehicles," *IEEE Journal of Emerging and Selected Topics in Power Electronics*, vol. 3, no. 1, pp. 50–64, 2015.

[22] T. Nakata, N. Takahashi, K. Fujiwara, and A. Ahagon, "Periodic boundary condition for 3-d magnetic field analysis and its applications to electrical machines," *IEEE Transactions on Magnetics*, vol. 24, no. 6, pp. 2694–2696, 1988.

[23] F. Y. Lin, G. A. Covic, and J. T. Boys, "Evaluation of magnetic pad sizes and topologies for electric vehicle charging," *IEEE Transactions on Power Electronics*, vol. 30, no. 11, pp. 6391–6407, 2015.

[24] T. Diekhans and R. W. De Doncker, "A dual-side controlled inductive power transfer system optimized for large coupling factor variations and partial load," *IEEE Transactions on Power Electronics*, vol. 30, no. 11, pp. 6320–6328, 2015.

[25] S. Bandyopadhyay, V. Prasanth, P. Bauer, and J. Ferreira, "Multi-objective optimisation of a 1-kw wireless ipt systems for charging of electric vehicles," in *Transportation Electrification Conference and Expo (ITEC)*, pp. 1–7, IEEE, 2016.

[26] K. Peng and E. Santi, "Performance projection and scalable loss model of sic mosfets and sic schottky diodes," in *Electric Ship Technologies Symposium (ESTS)*, pp. 281–286, IEEE, 2015.

[27] Y. Del Valle, G. K. Venayagamoorthy, S. Mohagheghi, J.-C. Hernandez, and R. G. Harley, "Particle swarm optimization: basic concepts, variants and applications in power systems," *IEEE Transactions on evolutionary computation*, vol. 12, no. 2, pp. 171–195, 2008.

[28] C.-S. Wang, G. A. Covic, and O. H. Stielau, "Power transfer capability and bifurcation phenomena of loosely coupled inductive power transfer systems," *IEEE transactions on industrial electronics*, vol. 51, no. 1, pp. 148–157, 2004.

[29] J. Lin, R. Saunders, K. Schulmeister, P. Söderberg, A. Swerdlow, M. Taki, B. Veyret, G. Ziegelberger, M. H. Repacholi, R. Matthes, *et al.*, "Icnirp guidelines for limiting exposure to time-varying electric and magnetic fields (1 hz to 100 khz).," *Health Physics*, vol. 99, pp. 818–836, 2010.

[30] F. Y. Lin, G. A. Covic, and J. T. Boys, "Evaluation of magnetic pad sizes and topologies for electric vehicle charging," *IEEE Transactions on Power Electronics*, vol. 30, no. 11, pp. 6391–6407, 2015.